Energy-Based Modeling and Control of a Piezotube Actuated Optical Fiber

Edgar Ayala Perez, Yongxin Wu, Kanty Rabenorosoa, Yann Le Gorrec

Energy-based modeling and control of a piezo tube actuated optical fiber

Edgar Ayala Pérez, Yongxin Wu, *Member, IEEE,* Kanty Rabenorosoa, *Member, IEEE,* Yann Le Gorrec, *Senior Member, IEEE*

***Abstract*—This paper presents an energy-based modeling and control design method for a piezo tube actuated optical fiber. A non-linear infinite dimensional port Hamiltonian (pH) formulation of the 3D flexible optical fiber is derived from the Cosserat rod dynamical equations. Then the proposed infinite dimensional model is discretized using a pH structure and passivity preserving discretization method for the simulation and control design. This model is then validated against experimental data obtained using a built-in experimental setup equipped with a MEMS Analyzer. A complete pH formulation of the piezo tube actuated optical fiber is proposed, combining the Cosserat rod model and actuator dynamics. This model is used for the end-point path control design using an interconnection and damping assignment passivity based control (IDA-PBC) method. Both the proposed pH model of the overall system and the controller are validated in simulation and against experimental results.**

***Index Terms*—Cosserat rod, piezo tube, port Hamiltonian systems, optical fiber.**

I. Introduction

THE range of medical applications of continuum robots has been growing in the last past years. The main purpose of using these robots is to perform minimally invasive surgeries to reduce the potential risks of damage and to improve the success of the involved procedures in surgeries [1]. Some examples of important surgeries and problems solved with continuum robots are given hereafter. Neurosurgical interventions in which wide cranium openings are done. In this type of interventions, tissue is pushed aside to gain access to deeper regions of the brain and proximity of the structures where important functionalities could exist. Oto-rhino-laryngology is usually performed with straight or flexible endoscopes and other instruments entering to the nostrils, mouth or ears [2]–[4]. Applications of continuum robots also include the development of scanning fiber endoscopes for optical coherence tomography (OCT) as presented in [5]. Scanning and imaging continuum robots are often used for cancer detection, microvascular oxygen tension measurement, chronic mesenteric ischemia, subcellular molecular interactions, etc [6]. However, due to the complexity of the continuum robots and their work environment, the actuation and control problems of continuum robots are difficult to handle.

This work has been supported by the EIPHI Graduate School (contract: ANR-17-EURE-0002) and ANR IMPACTS project (contract: ANR-21-CE48-0018).

Edgar Ayala Perez, Yongxin Wu, Kanty Rabenorosoa, Yann Le Gorrec are with the FEMTO-ST Institute, Univ. Bourgogne Franche-Comté, CNRS, 24 rue Savary, F-25000 Besançon, France. France (e-mail: yongxin.wu@femto-st.fr).

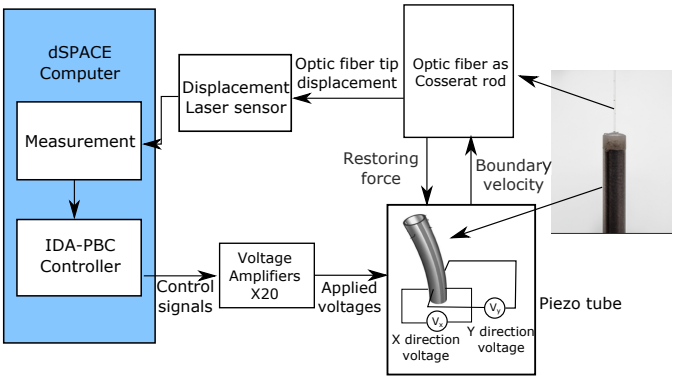

Fig. 1: System description of piezo tube actuated optical fiber and equipment for the control purpose.

The main objective of this work is to develop a first proof of concept of actuated scanning / imagining system, including modeling and control design. The proposed system can be used for both imaging and laser surgery at the tip of an endoscope for medical uses. The proposed model consists of an optical fiber rod clamped on and actuated through a piezo tube and the working principle of this experimental setup is described in Fig. 1. The piezo tube is the model PT230.94 with 33mm length, 3.2mm outer diameter and 2.2mm inner diameter. This actuator can move in the two directions X and Y by applying independent voltages on the two pairs of electrodes. The optical fiber (30mm length and 126μm radius) is clamped one the pizeo tube actuator as shown in the right picture of Fig. 1. The X- and Y- directions motion of the actuator generates the two-axial motion of the fiber.

The motion of the optical fiber exhibits large deformations, high flexibility and a nonlinear behavior. In a first approximation the Euler-Bernoulli beam assumption has been considered in the scanning optical fiber modeling in [7]–[9]. The piezo tube actuator has been used to generate the motion of the fiber in [7], [8] but only with a quasi-static model. In this paper, we propose to use Cosserat rod model [10] to describe the mechanical behavior of the optical fiber and a simple dynamic model for the piezo tube actuator. Cosserat rod formulations can be used to represent the non-planar and nonlinear dynamics of elastic rods that have a length greater than radius. It is widely used for the modeling of continuum robots [10]–[12]. Cosserat model exhibits a rich set of geometric strain (e.g., shear and torsion) and it is then particularly well adapted for the modeling of the considered optical fiber. In order to deal with the multiphysical nature of

this system and the interconnection between its constitutive elements, *i.e.* the rod and the piezo tube, the port Hamiltonian (pH) framework is used. The pH formulation consists in representing the system as the interconnection of three types of ideal elements: dynamical energy-storing elements, static energy-dissipating elements, and static lossless energy-routing elements [13]. They are linked through a central energy-routing structure, geometrically defined as a Dirac structure [14]. The basic and most important property of a Dirac structure is the power conservation. pH formulations are then particularly well adapted for the modeling and control of nonlinear multi-physical systems [15]. The pH approach has been generalized to the distributed parameter systems which are described by partial differential equations (PDEs) and their applications [16], [17], [18], [19]. Due to these advantages, the pH framework is suitable to model the PDEs of the Cosserat rod dynamics interconnected with the piezo tube actuator. Futhermore, the energy based modeling leads to a modular representation of interconnected systems. It is particularly well suited for control design through the use of the energy function, leading to controller and control design techniques with clear physical interpretation. Passivity based control design techniques have been first introduced for the control of Euler-Lagrange systems in [20]. They have then been generalized to pH systems through the Interconnection and Damping Assignment-Passivity Based Control (IDA-PBC) [21] method. The control of soft manipulators/actuators using IDA-PBC methods and lumped parameter models has been first introduced in [22]–[25]. In this work, we employ the IDA-PCB method to control the end-tip position of the piezo actuated optical fiber modeled as a set of interconnected pH systems.

The main contributions of the proposed work are: first, a pH representation of the optical fiber as a dynamic thin rod is derived based on Cosserat rod model proposed in [10], [26], [27] and validated through numerical simulations and experimental results. Furthermore a pH model of the optical fiber interconnected to the piezo tube actuator is obtained in a structure preserving way. This model is based on the principle of energy conservation and exhibits the system properties and provides a clear physical interpretation for control design. Second, the IDA-PBC method [21] is employed to achieve efficient and accurate regulation of the rod endpoint position for scanning purposes. Both, the proposed pH formulation and control law are numerically and experimentally validated.

This paper is organized as follows: in Section II the pH formulation of the optical fiber as a dynamic thin rod is proposed based on the Cosserat rod model. It is then validated using numerical simulations and experimental data. In Section III the piezo tube model is formulated using the pH framework and connected to the optical fiber in a power preserving way. Trajectory tracking control design is then investigated using passivity based control techniques in Section IV and the simulation and experimental results are presented to show the effectiveness of the proposed control strategy. Finally, conclusions and perspectives are given in Section V.

II. Port Hamiltonian Modeling of Cosserat rod for the Optical Fiber

A. Basics of Cosserat Rod Dynamics for the Optical Fiber

In this section, the optical fiber is considered as a slender rod which can be approximated as a one dimensional beam under classical Cosserat's elastic theory [28]. The rod of length L is characterized by its centerline curve $p(s,t) \in \mathbb{R}^3$ and its material orientation $\Phi(s,t) \in SO(3)$ as functions of the arc length ($s \in [0\ L]$) and time t. The complete set of partial differential equations describing the dynamic behavior of the Cosserat rod and the way they are derived can be found in [12], [10], [28] and [29]. They are summarized and adopted in this paper in the system of equations (1)[1,2]

$$\begin{cases} p_s &= \Phi v \\ \Phi_s &= \Phi \hat{u} \\ n_s &= \rho A \Phi(\hat{w}q + q_t) - f \\ m_s &= \rho\Phi(\hat{\omega}\mathcal{I}\omega + \mathcal{I}\omega_t) - \hat{p}_s n - l \\ q_s &= v_t - \hat{u}q + \hat{\omega}v \\ \omega_s &= u_t - \hat{u}\omega. \end{cases} \tag{1}$$

The partial derivative of p with respect to the arc length in the local frame is denoted by v, that is $v = \Phi^T p_s$. In the same way, the local frame curvature is denoted by $u = (\Phi^T \Phi_s)^\vee$ where the operator $(\cdot)^\vee$ maps from $\mathfrak{so}(3)$ to $\mathbb{R}^3$ [30]. The internal force and internal momentum are noted as n and n. The operator $(\cdot)^\wedge$ or $\hat{\cdot}$ maps from $\mathbb{R}^3$ to $\mathfrak{so}(3)$, *e.g.*

$$\hat{u} = \begin{bmatrix} 0 & -u_3 & u_2 \\ u_3 & 0 & -u_1 \\ -u_2 & u_1 & 0 \end{bmatrix}.$$

$q = \Phi^T p_t$ and $\omega = (\Phi^T \Phi_t)^\vee$ are the velocity and angular velocity in the local frame. The notations f and l stand for the distributed force and moment acting on the rod. The physical parameters of the rod are the material density ρ, the cross sectional area A, the second mass moment of inertia tensor $\mathcal{I}$. The linear elastic laws with material damping are chosen as the material constitutive laws:

$$\begin{aligned} n &= \Phi\left[K_{se}(v - v^*) + B_{se}v_t\right], \\ m &= \Phi\left[K_{bt}(u - u^*) + B_{bt}u_t\right] \end{aligned} \tag{2}$$

where the "se" subscript stands for shear and extension and "bt" stands for bending and torsion. v^* stands for the initial state of the shear and axial elongation, and u^* represents the initial bending and torsion (curvature). In this work we consider that the initial position of the optical fiber is a straight rod *i.e.*, $v^* = (0,0,1)^T$ and $u^* = (0,0,0)^T$. $K_{se} \in \mathbb{R}^{3\times3}$ is the stiffness matrix for shear and extension. $K_{bt} \in \mathbb{R}^{3\times3}$ is the stiffness matrix for bending and twisting. The matrices B_{se}, $B_{bt} \in \mathbb{R}^{3\times3}$ are the Kelvin-Voigt type viscous damping matrices which depend on the material properties and cross-sectional geometry. More details can be found in [31].

[1]For the sake of simplicity, the spatial and time variables (s,t) are omitted over the paper unless it causes confusion.

[2]p_s and p_t stand for the partial derivative of p with respect to the arc length $\frac{\partial p}{\partial s}$ and with respect to time $\frac{\partial p}{\partial t}$, respectively.

B. PH Modeling of Cosserat Rod

The main purpose of this section is to derive from Cosserat's rod dynamic equations (1) and proper definition of the energy, a port Hamiltonian formulation of the optical fiber rod. For that purpose we choose as state variables, the energy variables *i.e.* the extensive variables of Thermodynamics. The first energy variable is the difference of shear and axial elongation between the original and deformed states as in equation (3). The second state variable is the internal translational momentum of the rod that depends on the cross-sectional area A and the linear velocity q of the material as in equation (4).

$$x_1 = v - v^*, \tag{3}$$
$$x_2 = \rho A p_t = \rho A q. \tag{4}$$

The third state variable is the difference in bending and torsion (curvature) between the original and deformed states of the rod as in equation (5). The fourth energy variable is the internal rotational momentum of the rod that is related to the inertia $\mathcal{I}$ and the angular velocity ω as in Equation (6).

$$x_3 = u - u^*, \tag{5}$$
$$x_4 = \rho \mathcal{I} \Phi_t = \rho \mathcal{I} \omega. \tag{6}$$

The total mechanical energy is equal to the sum of the potential elastic energy and kinetic energy of the rod. The potential elastic energy relates the first energy variable of equation (3) with the shear and extension stiffness matrix K_{se} and the third energy variable of equation (5) with the bending and torsion stiffness matrix K_{bt}. The kinetic energy, which includes the internal translational and rotational momentum of the rod, contains the second energy variable of equation (4) and the fourth energy variable of equation (6). Finally the total energy (Hamiltonian function) is expressed as follows:

$$\begin{aligned}\mathcal{H}(x) &= \frac{1}{2}\int_0^L [K_{se}x_1^2 + K_{bt}x_3^2 + \frac{1}{\rho A}x_2^2 + \frac{1}{\rho \mathcal{I}}x_4^2]\, ds \\ &= \frac{1}{2}\int_0^L [(K_{se}(v-v^*)^2 + K_{bt}(u-u^*)^2 \\ &\qquad + \rho A q^2 + \rho \mathcal{I}\omega^2]\, ds \\ &= \frac{1}{2}\int_0^L x^T \mathcal{L} x\, ds\end{aligned} \tag{7}$$

where the state (energy) variable $x = (x_1, x_2, x_3, x_4)^T$ and

$$\mathcal{L} = \text{diag}\begin{bmatrix} K_{se} & \frac{1}{\rho A} & K_{bt} & \frac{1}{\rho \mathcal{I}} \end{bmatrix}. \tag{8}$$

Remark 1. *The stiffness matrices K_{se} and K_{bt} can be extended to nonlinear elasticity and depend on the shear and axial elongation v and the bending and torsion u. This extension does not change the structure of proposed PH representation of the Cosserat rod and it only changes the constitutive laws and co-energy variables in (9) and (11). To our best knowledge, most of Cosserat rod models in the literature deal with the linear elastic laws which provides enough accuracy hence we keep the linear stiffness in this work.*

The co-energy variables e associated to the energy variables x are defined by the variational derivative of the Energy with respect to the state $e = \delta_x \mathcal{H}(x) = \mathcal{L}x$. The first co-energy variable which is related to the shear and elongation of the rod x_1, is the force on the local frame (9). The second co-energy variable that is related to the internal translational momentum x_2 is the local velocity as shown in equation (10).

$$e_1 = K_{se}x_1 = K_{se}(v - v^*), \tag{9}$$
$$e_2 = \frac{1}{\rho A}x_2 = \frac{1}{\rho A}\rho A q = q. \tag{10}$$

The third co-energy variable, related with the bending and torsion is shown in equation (11). In the same way, the fourth co-energy variable presented in equation (12) is related to the internal rotational momentum.

$$e_3 = K_{bt}x_3 = K_{bt}(u - u^*), \tag{11}$$
$$e_4 = (\rho \mathcal{I})^{-1}x_4 = (\rho \mathcal{I})^{-1}\rho \mathcal{I}\omega = \omega. \tag{12}$$

The Cosserat's rod model can be written in the port Hamiltonian framework with distributed input as in [32]:

$$\begin{aligned}\dot{x} &= (J - R)\delta_x \mathcal{H}(x) + g u_d \\ y_d &= g^T \delta_x \mathcal{H}(x)\end{aligned} \tag{13}$$

where x is the vector of aforementioned state (energy) variables and $\delta_x \mathcal{H}(x) = \mathcal{L}x$ the vector of co-energy variables. The input vector $u_d = \begin{bmatrix} f & l \end{bmatrix}^T$ is composed of the distributed force and distributed moment. $J = \mathcal{J}_{lin} + J_{nl}$ is a formally skew symmetric operator

$$J = \underbrace{\begin{bmatrix} 0 & \frac{\partial}{\partial s} & 0 & 0 \\ \frac{\partial}{\partial s} & 0 & 0 & 0 \\ 0 & 0 & 0 & \frac{\partial}{\partial s} \\ 0 & 0 & \frac{\partial}{\partial s} & 0 \end{bmatrix}}_{\mathcal{J}_{lin}} + \underbrace{\begin{bmatrix} 0 & \hat{u} & 0 & \hat{v} \\ \hat{u} & -\rho A \hat{\omega} & 0 & 0 \\ 0 & 0 & 0 & \hat{u} \\ \hat{v} & 0 & \hat{u} & -\rho J \hat{\omega} \end{bmatrix}}_{J_{nl}}. \tag{14}$$

The operator $\mathcal{J}_{lin}$ is skew-symmetric when the boundary variables are chosen properly [17]. The matrix J_{nl} is skew-symmetric since $\hat{u}, \hat{\omega} \in \mathfrak{so}(3)$ are skew-symmetric and ρ, A and $\mathcal{I}$ are constant parameters. The dissipation operator $R = R^T \geq 0$ and the input map g are defined as

$$R = \begin{bmatrix} 0 & 0 & 0 & 0 \\ 0 & B_{se} & 0 & 0 \\ 0 & 0 & 0 & 0 \\ 0 & 0 & 0 & B_{bt} \end{bmatrix}; g = \begin{bmatrix} 0 & 0 \\ \mathcal{I}^T & 0 \\ 0 & 0 \\ 0 & \mathcal{I}^T \end{bmatrix}. \tag{15}$$

The output $y_d = g^T \delta_x \mathcal{H}(x)$ is the power conjugate variable of the input u_d, *i.e.*, $y_d = \begin{bmatrix} \mathcal{I}^T q & \mathcal{I}^T \omega \end{bmatrix}^T = \begin{bmatrix} p_t & \mathcal{I}_t \end{bmatrix}^T$.

We define the boundary port variable of the pH rod model (13) using the co-energy variables at the boundaries in $s = 0$ and $s = L$

$$\begin{bmatrix} f_\partial \\ e_\partial \end{bmatrix} = \begin{bmatrix} e_\partial^1 \\ e_\partial^2 \\ e_\partial^3 \\ e_\partial^4 \end{bmatrix}\Bigg|_{\partial = 0, L}. \tag{16}$$

In this paper, the optical fiber rod is clamped to the piezo tube which leads to a clamped-free boundary condition with the velocity input on the clamped side ($s = 0$). From the

boundary conditions, one can define the boundary input of the rod as follows:

$$u_b = [e_2(0), e_4(0), e_1(L), e_3(L)]^T \tag{17}$$

i.e. velocity and angular velocity at the clamped side ($s = 0$) and the force and moment at the free side ($s = L$). The boundary output are chosen as the power conjugated boundary port variables *i.e.*

$$y_b = [e_1(0), -e_3(0), -e_2(L), e_4(L)]^T. \tag{18}$$

The energy balance equation associated to this system reads:

$$\begin{array}{rcl} \frac{\partial \mathcal{H}}{\partial t}(x) & = & \int_0^L (-\delta_x \mathcal{H}^T R \delta_x \mathcal{H} + y_d^T u_d)\, ds \; + y_b^T u_b \\ & \leq & \int_0^L y_d^T u_d \, ds \; + y_b^T u_b. \end{array} \tag{19}$$

For more details on the parametrization of the boundary variables, the readers can refer to [17]. In this work, we consider that the optical fiber is controlled through the piezo tube motion acting on its boundary conditions and in this case the distributed force and moment acting on the rod are equal to zero, *i.e.* $u_d = \begin{bmatrix} f & l \end{bmatrix}^T = 0$.

C. Spatial Discretization and Numerical Validation

The differential part of the skew symmetric operator, $\mathcal{J}_{lin}$, is discretized in space following the procedure of [33] where the concept of staggered grids is introduced. For the sake of the simplicity, we first introduce the variable $f_r = \mathcal{J}_{lin} e$. We have the following relation:

$$\begin{bmatrix} f_{r1} \\ f_{r2} \\ f_{r3} \\ f_{r4} \end{bmatrix} = \begin{bmatrix} 0 & \frac{\partial}{\partial s} & 0 & 0 \\ \frac{\partial}{\partial s} & 0 & 0 & 0 \\ 0 & 0 & 0 & \frac{\partial}{\partial s} \\ 0 & 0 & \frac{\partial}{\partial s} & 0 \end{bmatrix} \begin{bmatrix} e_1 \\ e_2 \\ e_3 \\ e_4 \end{bmatrix}. \tag{20}$$

The spatial resolution h and the number of discretization points n are chosen such that $(n + \frac{1}{2})h = L$. The first part of the system is discretized over the grid presented in Figure 2 for x_1 and x_2. A similar grid is used for the discretization of x_3 and x_4.

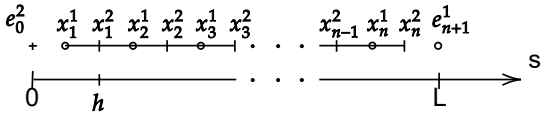

Fig. 2: Staggered grid for a clamped-free rod

In this discretized model, the state variables are ordered following the vector $x_d = [x_d^1\ x_d^2\ x_d^3\ x_d^4]^T \in \mathbb{R}^{4n}$ where the discretized energy variables are defined as $x_d^i = [x_1^i \dots x_n^i]^T$, with $i = 1, 2, 3, 4$ where the $x_k^i (k \in \{1 \dots n\})$ are the approximations of the state variables respectively evaluated at $s = \{(k-1)h,\ (k-0.5)h\}$. e_0^2, e_0^4, e_{n+1}^1 and e_{n+1}^3 denote the boundary conditions at the clamped base and at the free tip of the rod. The vector of discretized co-energy variables is defined as

$$\begin{bmatrix} e_k^1 \\ e_k^2 \\ e_k^3 \\ e_k^4 \end{bmatrix} = \mathcal{L}_k \begin{bmatrix} x_k^1 \\ x_k^2 \\ x_k^3 \\ x_k^4 \end{bmatrix} \tag{21}$$

and thus, by central approximation of the spatial derivative equation (22) appears,

$$\begin{bmatrix} f_k^1 \\ f_k^2 \\ f_k^3 \\ f_k^4 \end{bmatrix} = \frac{1}{h} \begin{bmatrix} e_{k+1}^2 - e_k^2 \\ e_k^1 - e_{k-1}^1 \\ e_{k+1}^3 - e_k^3 \\ e_k^4 - e_{k-1}^4 \end{bmatrix}. \tag{22}$$

From which the vector $f_d = [f_d^1\ f_d^2\ f_d^3\ f_d^4]^T$ could be expressed as an approximation of equation (20). In this way the matrices shown in equations (23) and (24) could be found for a clamped-free rod as in [18]

$$f_d^1 = \underbrace{\frac{1}{h} \begin{bmatrix} 1 & & & \\ -1 & 1 & & \\ & \ddots & \ddots & \\ & & -1 & 1 \end{bmatrix}}_{D} e_d^2 + \frac{1}{h} \begin{bmatrix} -1 \\ 0 \\ \vdots \\ 0 \end{bmatrix} e_0^2, \tag{23}$$

$$f_d^2 = \underbrace{\frac{1}{h} \begin{bmatrix} -1 & 1 & & \\ & \ddots & \ddots & \\ & & -1 & 1 \\ & & & -1 \end{bmatrix}}_{-D^T} e_d^1 + \frac{1}{h} \begin{bmatrix} 0 \\ \vdots \\ 0 \\ 1 \end{bmatrix} e_{n+1}^1. \tag{24}$$

Similarly, this discretization should be done for the second pair f_d^3 and f_d^4. This leads to the final port Hamiltonian representation:

$$\begin{bmatrix} \dot{x}_d^1 \\ \dot{x}_d^2 \\ \dot{x}_d^3 \\ \dot{x}_d^4 \end{bmatrix} = \left[\underbrace{\begin{bmatrix} 0 & D & 0 & 0 \\ -D^T & 0 & 0 & 0 \\ 0 & 0 & 0 & D \\ 0 & 0 & -D^T & 0 \end{bmatrix} + \begin{bmatrix} 0 & \hat{u} & 0 & \hat{v} \\ \hat{u} & -\rho A \hat{\omega} & 0 & 0 \\ 0 & 0 & 0 & \hat{u} \\ \hat{v} & 0 & \hat{u} & -\rho J \hat{\omega} \end{bmatrix}}_{J_d} - \underbrace{\begin{bmatrix} 0 & 0 & 0 & 0 \\ 0 & B_{se} & 0 & 0 \\ 0 & 0 & 0 & 0 \\ 0 & 0 & 0 & B_{bt} \end{bmatrix}}_{R_d} \right] \underbrace{\begin{bmatrix} e_d^1 \\ e_d^2 \\ e_d^3 \\ e_d^4 \end{bmatrix}}_{e_d} + \underbrace{\frac{1}{h} \begin{bmatrix} g_1 \\ g_2 \\ g_3 \\ g_4 \end{bmatrix}}_{g_d} \underbrace{\begin{bmatrix} e_0^2 \\ e_{n+1}^1 \\ e_0^4 \\ e_{n+1}^3 \end{bmatrix}}_{u}; \tag{25}$$

$$\begin{bmatrix} y_1 \\ y_2 \\ y_3 \\ y_4 \end{bmatrix} = g^T \frac{\partial \mathcal{H}}{\partial x} = \frac{1}{h} \begin{bmatrix} g_1^T & g_2^T & g_3^T & g_4^T \end{bmatrix} \begin{bmatrix} e_d^1 \\ e_d^2 \\ e_d^3 \\ e_d^4 \end{bmatrix}$$

with

$$g_1 = \begin{bmatrix} -1 \\ 0 \\ \vdots \\ 0 \end{bmatrix}; g_2 = \begin{bmatrix} 0 \\ 0 \\ \vdots \\ 1 \end{bmatrix}; g_3 = \begin{bmatrix} -1 \\ 0 \\ \vdots \\ 0 \end{bmatrix}; g_4 = \begin{bmatrix} 0 \\ 0 \\ \vdots \\ 1 \end{bmatrix}.$$

The discretized energy function of the rod is given by

$$\mathcal{H}_d(x_d) = \frac{1}{2} x_d^T \mathcal{L}_d x_d. \tag{26}$$

Before proceeding to the experimental identification of the considered system, we first propose to validate the pH Cosserat rod model with the existing results in the literature. To this end, the discretized pH model (25) is compared with the numerical schemes used for simulation of the Cosserat's rod using the

code proposed in [29]. For these numerical simulations we used the parameters of the rod given in Table I, the rod being divided in 40 elements. A force of $[0.5\ 0\ 0]N$ at the tip is first

TABLE I: Main rod's parameters

Parameter	Value	Units
Length (L)	0.4	m
Young's modulus (E)	207	GPa
Radius (r)	0.0012	m
Density (ρ)	8000	kg/m^3

applied as initial condition, and then released. Fig. 3 shows the displacements of the rod's tip versus time for the port Hamiltonian model and the Cosserat rod model presented in [10]. Figure 3 shows that the results obtained using these two

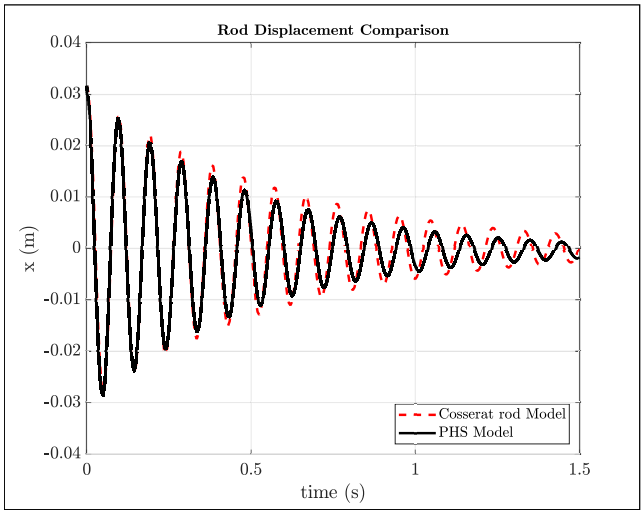

Fig. 3: Comparison between the port Hamiltonian rod model and the Cosserat rod model

are in global accordance with almost 86% curve fitness. The small differences in the behavior of the two systems is due to the natural damping of the different integration methods that are used.

D. Optical Fiber Parameters Identification

We consider now the experimental validation of the proposed pH model of the optical fiber. Some physical parameters of the fiber, such as the one associated to its geometry (length, radius) or to its composition (material density or Young's modulus), are supposed to be known. However, the dissipation coefficients B_{se} and B_{bt} are unknown and need to be identified. In this respect, some experimental measurements of the tip displacement of the optical fiber are performed. These measurements are obtained using a MEMS Analyzer *Polytec MSA-500* (see Figure 4a) using the experimental setup of Figure 4b.

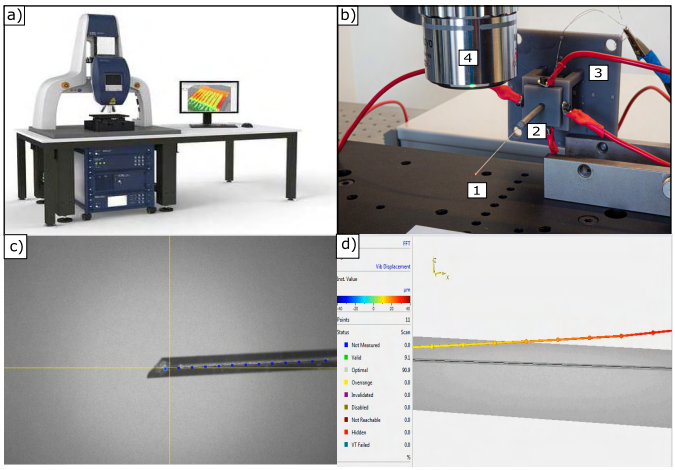

Fig. 4: Experimental setup: a) Polytec MSA-500 analyzer; b) Experimental setup. 1: Optical fiber; 2: piezo tube; 3: 3D printed base; 4: 2X Mitutoyo objective; c) Optical fiber position tracking under the MEMS Analyzer; d) Optical fiber motion measurement by Laser Doppler Vibrometry (LDV).

The MEMS Analyzer (Polytec MSA-500, Fig. 4 a)) measures the displacement using out of plane vibration Laser Doppler Vibrometry (LDV). An Arduino UNO is programmed to send $3, 4$ and 5 volts to a $20X$ voltage amplifier to obtain $60, 80$ and 100 volts respectively to move the piezo tube and the optical fiber to an initial position. Then this voltage is turned off (0 volts) to release the fiber, and simultaneously, a TTL signal is sent to the MEMS analyzer. This TTL signal is used as a trigger signal for the measurement. The motion of different points on the optical fiber Fig. 4 c) are measured by the Laser Doppler Vibrometry of the MEMS Analyzer as shown in Fig. 4 d).

We consider that the parameters given in table II are fixed from the optical fiber's mechanical properties.

TABLE II: Fixed Parameters

Parameter	Value	Units
Young's modulus (E)	9	GPa
Radius (r)	126	μm
Density (ρ)	1930	kg/m^3

The parameters to be identified are the ones associated with the dissipation occurring in the system *i.e.* the dissipation matrices. They are identified using the Matlab$^{@}$ function *fsolve* and the *Levenberg-Marquardt* algorithm. Simulations are done using 20 elements for the discretization.

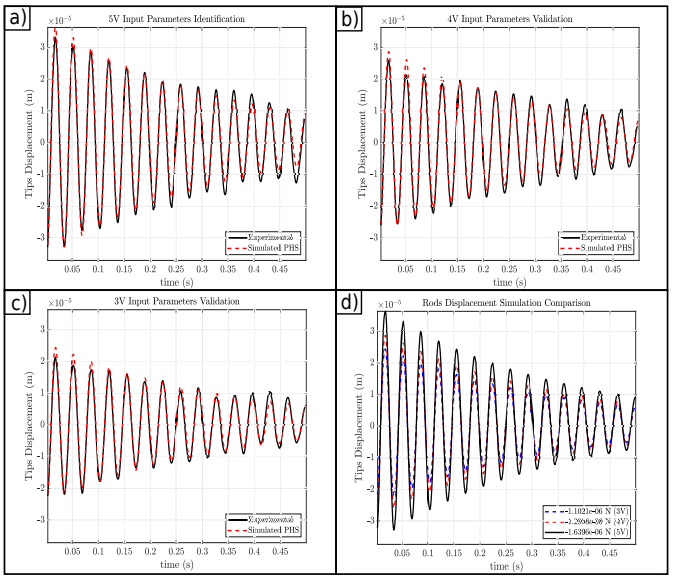

Fig. 5: Experimental measurements for optical fiber's parameters identification. a) 5V Input used for identification. b) 4V Input validation. c) 3V Input validation. d) 3V, 4V and 5V simulation comparison

The displacement obtained for a $5V$ input, as shown in Figure 5a, is used to identify the parameters. The fitting percentage between the identified model and the experimental measurement is over 90%. The resulting shear and extension matrix and bending and torsion matrix are given respectively by:

$$B_{se} = \text{diag}\begin{bmatrix}10.9e-7 & 9.9e-7 & 6.0e-7\end{bmatrix}\text{Ns}; \quad (27)$$

$$B_{bt} = \text{diag}\begin{bmatrix}4.7e-7 & 3.4e-7 & 13.4e-7\end{bmatrix} textNm^2\text{s}. \quad (28)$$

The model is then validated using a $3V$ and $4V$ input as shown in Figure 5b and 5c, respectively. These curves fitting percentage are both over 88%. Finally a comparison between the three simulations is given in Figure 5d.

III. Modeling of the Piezo Tube Actuated Optical Fiber

The piezo tube actuated optical fiber shown in Figure 6 includes a four legged base for the continuum robot, a four degrees adjustable base for the sensors, a $20X$ voltage amplifier and two Keyence sensors that measure the displacements of the actuator and of the rod's tip. The continuum robot and its simplified scheme are shown in Figure 7. The communication interface is designed using *Simulink/Control Desk* and *dSpace* controller board.

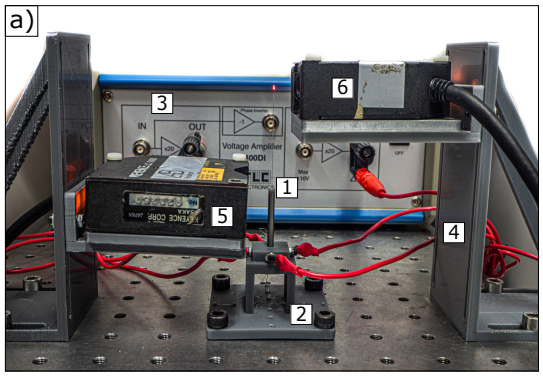

Fig. 6: a) 1: piezo tube actuated optical fiber; 2: four legged base; 3: A400DI voltage amplifier; 4: four degrees adjustable support; 5: Keyence displacement sensor for piezo tube actuator position measurement; 6: Keyence displacement sensor for optical fiber tip measurement.

A. PH Modeling of piezo tube Actuator and Interconnected System

For control design purpose, and for a sake of simplicity, the piezo tube actuator is considered as a simple spring-mass-damper system as shown in the right side of Figure 7 in this work. A voltage dependent force F_{pzt}(V) is applied to generate a displacement of the mass M of the actuator that is also subject to the restoring force from the rod $F_{rod} = e_0^1$. A stiffness coefficient K and a damping coefficient B are taken into account to cope with the piezo tube dynamics.

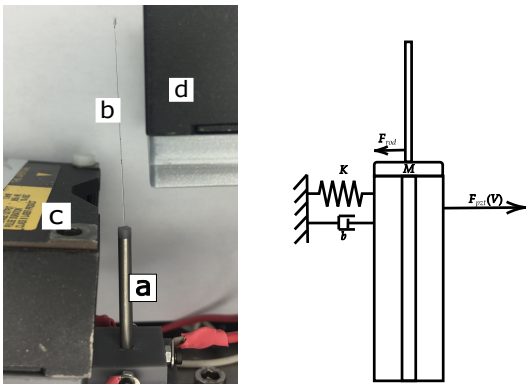

Fig. 7: Left: (a) piezo tube (b) actuated optical fiber (c),(d) Laser sensors. Right: Piezo tube modeled as a spring-mass-damper system for one direction, the other direction is the same as this model.

As for the optical fiber, the model is derived using the port Hamiltonian framework. The energy variables are the relative position p_{pzt} of the actuator and the momentum m_{pzt5pt}, defined in equation (29)

$$x_{p1} = p_{pzt}, \quad x_{p2} = m_{pzt}. \quad (29)$$

The Hamiltonian function is defined as the sum of the potential and kinetic energies as follows:

$$\mathcal{H}_{pzt} = \frac{1}{2}[Kx_{p1}^2 + \frac{1}{M}x_{p2}^2] = \frac{1}{2}[Kp_{pzt}^2 + \frac{1}{M}m_{pzt}^2]. \quad (30)$$

The co-energy variables are defined by

$$\begin{bmatrix} e_{p1} \\ e_{p2} \end{bmatrix} = \nabla \mathcal{H}_{pzt}(x_{pzt}) = \begin{bmatrix} K & 0 \\ 0 & \frac{1}{M} \end{bmatrix} \begin{bmatrix} x_{p1} \\ x_{p2} \end{bmatrix}. \tag{31}$$

Remark 2. *In this work, we consider the piezo tube actuation on both $x-$axis and $y-$axis are independent. Hence, the piezo tube dynamics can be modeled by two spring-mass-damper systems. Hence, the energy variables of the piezo tube $x_{p1}, x_{p2} \in \mathbb{R}^2$.*

The piezo tube actuator pH model reads

$$\begin{cases} \dot{x}_{pzt} &= (J_{pzt} - R_{pzt})\, e_{pzt} + g_{pzt} u_{pzt} + g_{pzt} u_{rod} \\ y_{pzt} &= g_{pzt}^T e_{pzt} \end{cases} \tag{32}$$

where:

$$J_{pzt} = \begin{bmatrix} 0 & I \\ -I & 0 \end{bmatrix}; R_{pzt} = \begin{bmatrix} 0 & 0 \\ 0 & b \end{bmatrix}; g_{pzt} = \begin{bmatrix} 0 \\ I \end{bmatrix}, \tag{33}$$

where $b \in \mathbb{R}^{2\times 2}$ is the damper matrix, I is the two by two identity matrix. The input $u_{pzt} = F(V)$ are the forces generated by the applied voltage on the piezo tube on $x-$ and $y-$ direction. u_{rod} are the restoring forces exerted by the rod at the clamped point ($s = 0$) for two directions. The output of the system are the velocities of the piezo tube that are also the boundary inputs of the optical fiber, *i.e.*, e_0^2. The interconnection relations between the piezo tube (32) and the discretized optical fiber rod (25) are given by

$$\begin{bmatrix} e_0^2 \\ u_{rod} \end{bmatrix} = \begin{bmatrix} 0 & I \\ -I & 0 \end{bmatrix} \begin{bmatrix} e_0^1 \\ y_{rod} \end{bmatrix}. \tag{34}$$

Finally, considering the above interconnection relations, the finite dimensional model of the overall system reads:

$$\underbrace{\begin{bmatrix} \dot{x}_{rod} \\ \dot{x}_{pzt} \end{bmatrix}}_{\dot{x}_t} = \underbrace{\left[\begin{array}{c|c} (J_d - R_d) & \mathcal{Z} \\ \hline \mathcal{C} & (J_{pzt} - R_{pzt}) \end{array}\right]}_{(J_t - R_t)} \underbrace{\begin{bmatrix} e_{rod} \\ e_{pzt} \end{bmatrix}}_{e_t} + g_{in}\mathbf{F}(V) \tag{35}$$

where $e_t = \nabla \mathcal{H}_t(x_d, x_{pzt})$, Hamiltonian function

$$\begin{aligned} \mathcal{H}_t &= \frac{1}{2}\left[K_{se}(v - v^*)^2 + \rho A q^2 + K_{bt}(u - u^*)^2 \right. \\ &\left. + \rho \mathcal{I} \omega^2 + K p_{pzt}^2 + \frac{1}{M} m_{pzt}^2 \right] \end{aligned} \tag{36}$$

and interconnection matrices:

$$\mathcal{Z} = \begin{bmatrix} g_1 & 0 \\ 0 & 0 \\ 0 & 0 \\ 0 & 0 \end{bmatrix}; \qquad \mathcal{C} = \frac{1}{h}\begin{bmatrix} 0 & 0 & 0 & 0 \\ -g_1^T & 0 & 0 & 0 \end{bmatrix}.$$

The input vector is given by:

$$g_{in} = \begin{bmatrix} 0 & 0 & 0 & 0 & 0 & 1 \end{bmatrix}^T.$$

As for the optical fiber, some physical parameters of the actuator need to be identified. The mass of the piezo tube plus optical fiber holder is approximately 1g. The parameters to be identified are the stiffness K, the damping b and the proportional gain linking the voltage to the force. In order to identify these parameters, a step input of 200V is applied to the actuator, and the parameters are identified using the *Matlab* function *lsqcurvefit*. The best fitting parameters are given in Table III.

TABLE III: Identified piezo tube's parameters

Parameter	Value	Units
Stiffness (K)	27.5713	N/m
Damping (b)	0.2821	Ns/m
Force factor	0.7557	V/N

Figure 8 shows the performances of the identified model with respect to the experimental measurement.

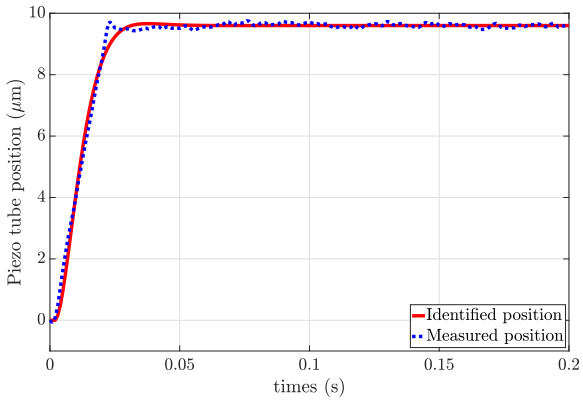

Fig. 8: Experimental measurements for piezo tube's parameters identification

It is well known that the piezo tube is subject to non-linearities such as hysteresis and creep phenomena [34]. In this work, the piezo tube actuator is approximated by a simple mass spring damper system, and the hysteresis and creep phenomena are not explicitly taken into account. Yet the hysteresis is accounted for in an indirect way through the parameters estimation of the Cosserat rod model. Indeed, the Cosserat rod model also exhibits an hysteretic behavior when it is controlled at one boundary of its spatial domain and the measurement occurs at the other boundary. The overall hysteretic behavior of the system is then considered during the identification process. The experimental data corresponding to the open loop response at different frequencies ($\{0.5, 1, 2, 5\}$Hz) is shown in Fig. 9. These results show that the proposed interconnected model allows to cope with the hysteretic behavior of the system while using a simple dynamic model for the piezo tube actuator at low frequency (< 1Hz). Thus, the proposed model can be used for the optical fiber regulation problem in a low frequency range. However, when a higher frequency signal is applied to the system, the simple piezo tube actuator model is not accurate enough to cope its hysteretic behavior. In this respect, a more accurate nonlinear model for the piezo tube actuator will be investigated in the future. Regarding now the creep effect: in this work, we limit the working conditions to small deformations in order to avoid this non linear phenomenon. Some experimental results showing the creep effect during small and large deformations is given in Fig. 10. With the small deformation limitation (under 10μm), we see that our model cope with the main dynamic behavior of the system. Furthermore, for the scanning and imaging

purposes, the system does not usually stay in the static position for a long time such that the creep can be neglected. The creep effects due to large deformations will also be investigated in the future.

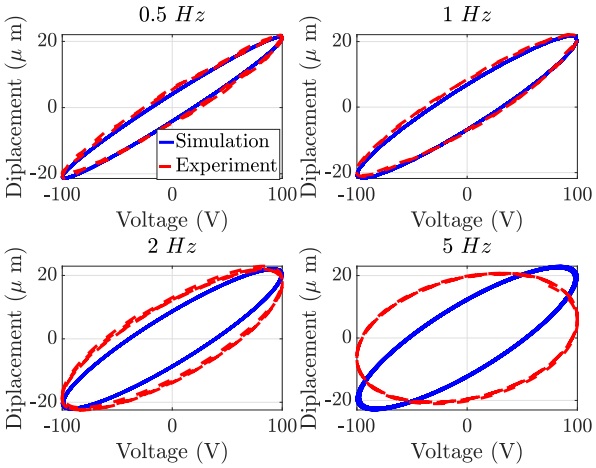

Fig. 9: Experimental and simulation comparison of the hysteresis phenomena

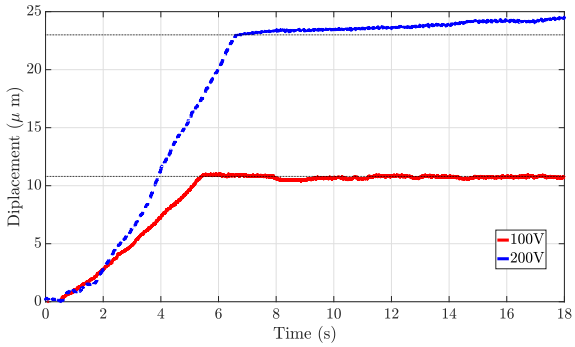

Fig. 10: Creep effect for the large displacement

IV. Position Control via IDA-PBC Method

In this section we consider the control of the end position of the optical fiber using the block diagram of Figure 11.

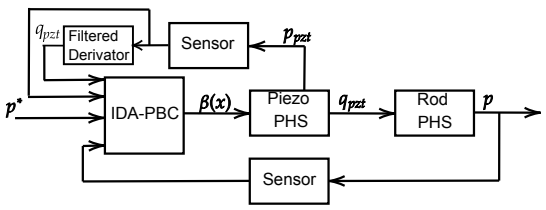

Fig. 11: Complete closed loop system block diagram

p^* is the desired output position. The controller uses as input the position and velocity of the piezo tube, p_{PZT} and p_{PZT} respectively, and the end position of the optical fiber p. The controller is first designed as a state feedback $u(x) = \beta(x)$ using the Interconnection and Damping Assignment-Passivity Based Control (IDA-PBC) design method in order to map the open loop system into the target system defined by

$$\dot{x} = (J_{cl} - R_{cl})\nabla H_{cl}. \tag{37}$$

in which $J_{cl} = -J_{cl}^T$ and $R_{cl} = R_{cl}^T \geq 0$ are the desired interconnection and dissipation matrices. The closed loop energy function H_{cl} is chosen such that

$$x^* = \arg\ \min H_{cl}(x^*) \tag{38}$$

where x^* is the desired equilibrium. The interconnection and dissipation matrices, and the energy of the closed loop system are chosen such that the matching equation

$$g^{\perp}\left[(J_{cl} - R_{cl})\frac{\delta H_{cl}}{\delta x} - (J - R)\frac{\delta H}{\delta x}\right] = 0 \tag{39}$$

is satisfied with $g^{\perp}$ a full rank annihilator of g *i.e.*, $g^{\perp}g = 0$. The resulting controller is then given by the relation:

$$\beta(x) = (g^T g)^{-1} g^T \left[(J_{cl} - R_{cl})\frac{\delta H_{cl}}{\delta x} - (J_t - R_t)\frac{\delta H_t}{\delta x_t}\right]. \tag{40}$$

In the present case we choose as annihilator:

$$g^{\perp} = \begin{bmatrix} I_n & 0 & 0 & 0 & 0 & 0 \\ 0 & I_n & 0 & 0 & 0 & 0 \\ 0 & 0 & I_n & 0 & 0 & 0 \\ 0 & 0 & 0 & I_n & 0 & 0 \\ 0 & 0 & 0 & 0 & I_n & 0 \end{bmatrix} \tag{41}$$

and the closed loop interconnection matrix as $J_{cl} = J_t$. The damping matrix is chosen to modify the damping of the piezo tube *i.e.* $R_{cl} = \text{diag}[0, B_{se}, 0, B_{bt}, 0, \tilde{b}]$. Then we can choose the desired closed loop Hamiltonian as follows

$$\begin{aligned} \mathcal{H}_{cl} = \frac{1}{2}\Big[&K_{se}(v - v^*)^2 + \rho A q^2 + K_{bt}(u - u^*)^2 \\ &+ \rho \mathcal{I}\omega^2 + \tilde{K}(p - p^*)^2 + \frac{1}{M}m_{pzt}^2\Big] \end{aligned} \tag{42}$$

in order to satisfy the matching equation (39) and to assign the desired equilibrium position as Eq (38). In (42), p^* and $\tilde{K}$ represent the desired position of the continuum robot and the desired stiffness used for energy shaping respectively.

Substituting (42) in (40) leads to the final control law

$$\beta(x) = \tilde{K}(p^* - p) + K p_{pzt} + (b - \tilde{b})q_{pzt}. \tag{43}$$

Remark 3. *One can see in* (43) *that the controller uses the velocity as input. This velocity is not measured and needs to be reconstructed from the position. In a first instance a numerical approximation of the derivation plus a low-pass frequency filter is used. An alternative approach consists in designing an observer to reconstruct the velocity.*

A. Numerical Validation

The first simulation that is performed consists in the position control in the 2-D $x-y$ space. In this case, a desired position of $[x, y] = [10, -10]\mu m$ is chosen. In Figure 12, the upper figures show both end-point trajectories (red lines) and desired positions (blue lines) in $x-$ (left figure) and $y-$ (right figure) axis. The bottom figure shows the error between the desired

position and the current position of the system. One can see the desired position can be reached in 1 second.

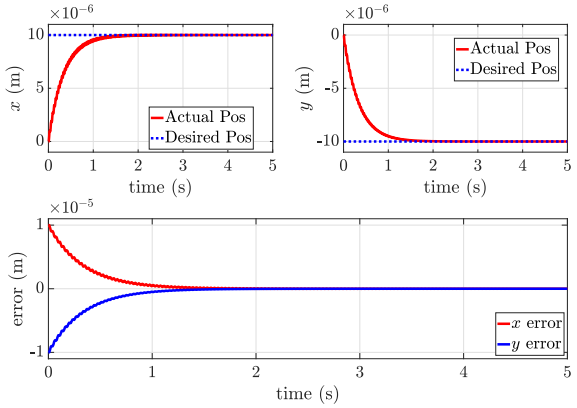

Fig. 12: $10\mu m$ and $-10\mu m$ Desired position simulated response

The second numerical validation consists in the regulation of the successive desired positions which are composed of 100 points with a spiral form. The position of the points on the trajectory are defined as

$$x_s = r_s \cos\phi_s; y_s = r_s \sin\phi_s \tag{44}$$

where r_s is the vector that contains radius elements linearly distributed on $[0,\ 5\mu m]$ and ϕ_s is the vector that contains angular element linearly distributed on $[0,\ 6\pi]$. Figure 13 shows the 100 desired positions on the spiral form (blue cross) and the controlled position (solid red line). One can see the optic fiber tip can follow the desired in a satisfactory way. It takes 45 seconds to move the tip position from the original point $[0, 0]\mu m$ to $[0, 5]\mu m$.

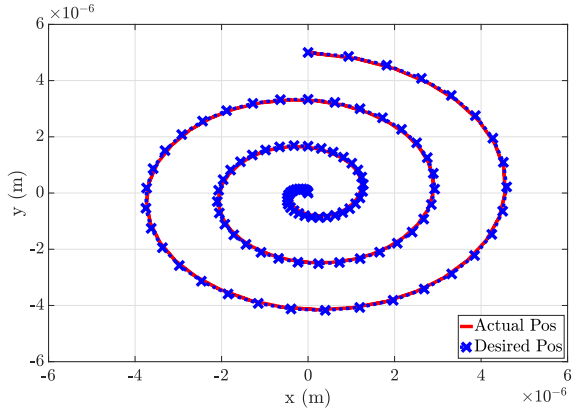

Fig. 13: Path following with a spiral

B. Experimental Validation

In this subsection we only consider the motion of the optical fiber in one direction. First we apply the IDA-PBC controller (43) with different values of the parameter $\tilde{K}$. The step responses of the closed loop system with different $\tilde{K} = 500, 1000, 2000, 5000$ are shown in Fig. 14 with desired position $5\mu m$. One can see that the time response becomes faster when $\tilde{K}$ is larger. When $\tilde{K} = 5000$, the closed loop response has an important overshoot. From the energy point of view, this parameter corresponds to the rod stiffness of the closed loop system. When the stiffness increases, the time response decreased but the overshoot increases too. In the considered example $\tilde{K} = 2000$ is a good compromise, the response is fast without overshot, hence, we will use this parameter for the controller afterwards.

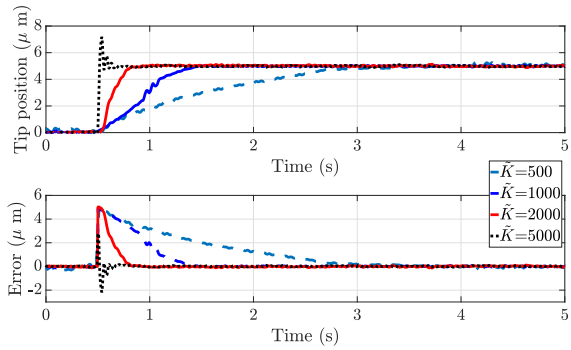

Fig. 14: Closed loop responses with different $\tilde{K}$

We compare the proposed IDA-PBC controller with a classic PD control with the same gain $\tilde{K} = 2000$ and derivative gain $\tilde{b} = 1$. In Fig. 15, one can see that the closed loop response for the PD controller (blue dotted line) is slower than the one with IDA-PBC (red solid line).

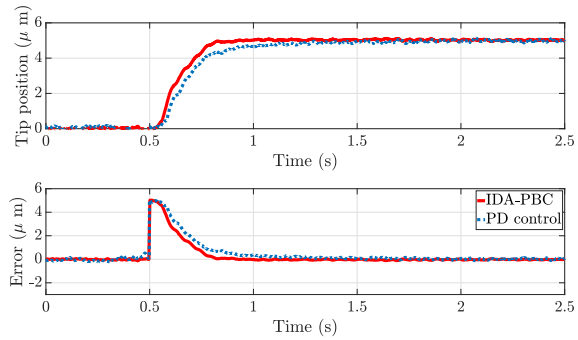

Fig. 15: Comparison between IDA-PBC control and PD control

Figure 16 shows the response of the closed loop system to $6\mu m$ set point position. From $t = 2s$, the desired position is defined at $5\mu m$ and the tip position reaches the desired position in less than $1s$. At $t = 4s$, the system is perturbed by an external disturbance caused by the working table movement. The tip position can still return to the desired position around $t = 6s$.

The last experimental validation consists in ramp position control. Figure 17 shows the desired position (blue dotted line in the upper figure), end point position (red solid line in the upper figure) and the error of tracking of the closed loop system (lower figure). The error remains in between $-0.5\mu m$ and $0.5\mu m$.

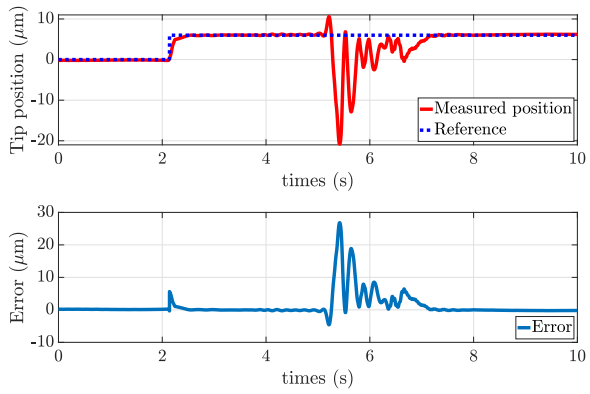

Fig. 16: Experimental validation with a perturbation

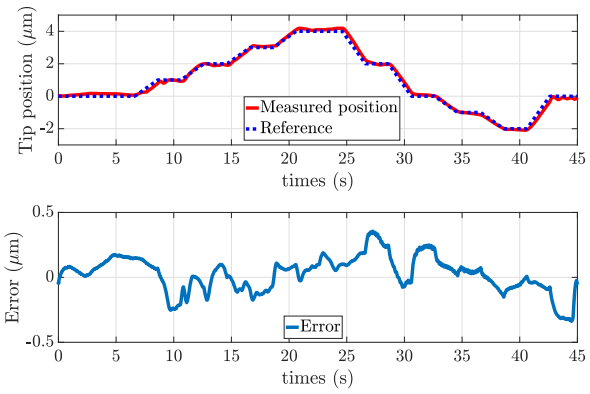

Fig. 17: Experimental optical fiber tip tracking of a desired reference and tracking error

V. Conclusion

This paper presents a port Hamiltonian approach for the modeling and control of a piezo tube actuated flexible optical fiber. The dynamics of the optical fiber is described by the Cosserat rod model and the piezo tube as a simple mass spring damper system in a first approximation. Taking the power conservation and modular nature of the pH representation, the overall model still keeps the pH structure which is useful for the control design. Based on the proposed pH model, an IDA-PBC method is developed to control the optical fiber's free end. Numerical simulations are done to validate both, the new proposed model and the controller. The controller simulation is performed in the 2D considering set point and trajectory control. At last, an experimental validation is performed. For that purpose, some key physical parameters are first identified. The controller is then validated using set point and trajectory control in the 1 direction. The experimental results show the efficiency of the controller even in presence of perturbations.

In future works, experimental validation in both [x, y] directions will be investigated. The nonlinear model model of the piezo tube actuator such as irreversible pH model [35] or Bouc-Wen model [36] will be considered in the future investigation. Furthermore, the proposed system will be integrated to bio-medical endoscopy application for scanning and imaging purpose.

References

[1] J. Burgner-Kahrs, D. C. Rucker, and H. Choset, "Continuum robots for medical applications:a survey," *IEEE Transactions on Robotics*, vol. 31, pp. 1261–1280, 2015.

[2] C. Girerd, A. V. Kudryavtsev, P. Rougeot, P. Renaud, K. Rabenorosoa, and B. Tamadazte, "Automatic tip-steering of concentric tube robots in the trachea based on visual slam," *IEEE Transactions on Medical Robotics and Bionics*, vol. 2, no. 4, pp. 582–585, 2020.

[3] D. V. A. Nguyen, C. Girerd, Q. Boyer, P. Rougeot, O. Lehmann, L. Tavernier, J. Szewczyk, and K. Rabenorosoa, "A hybrid concentric tube robot for cholesteatoma laser surgery," *IEEE Robotics and Automation Letters*, vol. 7, no. 1, pp. 462–469, 2022.

[4] L. S. Mattos, A. Acemoglu, A. Geraldes, A. Laborai, A. Schoob, B. Tamadazte, B. Davies, B. Wacogne, C. Pieralli, C. Barbalata, D. G. Caldwell, D. Kundrat, D. Pardo, E. Grant, F. Mora, G. Barresi, G. Peretti, J. Ortiz, K. Rabenorosoa, L. Tavernier, L. Pazart, L. Fichera, L. Guastini, L. A. Kahrs, M. Rakotondrabe, N. Andreff, N. Deshpande, O. Gaiffe, R. Renevier, S. Moccia, S. Lescano, T. Ortmaier, and V. Penza, "μralp and beyond: Micro-technologies and systems for robot-assisted endoscopic laser microsurgery," *Frontiers in Robotics and AI*, vol. 8, 2021.

[5] S. Moon, S.-W. Lee, M. Rubinstein, B. J. F. Wong, and Z. Chen, "Semi-resonant operation of a fiber-cantilever piezotube scanner for stable optical coherence tomography endoscope imaging," *Optics Express*, vol. 18(20), pp. 21 183–21 197, 2010.

[6] M. Kaur, P. M. Lane, and C. Menon, "Scanning and actuation techniques for cantilever-based fiberoptic endoscopic scanners—A Review," *Sensors*, vol. 21, p. 251, 2021.

[7] Q. Y. J. Smithwick, P. G. Reinhall, J. Vagners, and E. J. Seibel, "A Nonlinear State-Space Model of a Resonating Single Fiber Scanner for Tracking Control: Theory and Experiment ," *Journal of Dynamic Systems, Measurement, and Control*, vol. 126, no. 1, pp. 88–101, 04 2004.

[8] A. Rajiv, Y. Zhou, J. Ridge, P. G. Reinhall, and E. J. Seibel, "Electromechanical Model-Based Design and Testing of Fiber Scanners for Endoscopy," *Journal of Medical Devices*, vol. 12, no. 4, 09 2018.

[9] C. M. Brown, P. G. Reinhall, S. Karasawa, and E. J. Seibel, "Optomechanical design and fabrication of resonant microscanners for a scanning fiber endoscope," *Optical Engineering*, vol. 45, no. 4, pp. 043 001–, April 2006.

[10] J. Till, V. Aloi, and C. Rucker, "Real-time dynamics of soft and continuum robots based on Cosserat rod models," *The International Journal of Robotics Research*, vol. 38(6), pp. 723–746, 2019.

[11] F. Renda, M. Giorelli, M. Calisti, M. Cianchetti, and C. Laschi, "Dynamic model of a multibending soft robot arm driven by cables," *IEEE Transactions on Robotics*, vol. 30, no. 5, pp. 1109–1122, 2014.

[12] J. Till and D. C. Rucker, "Elastic rod dynamics: Validation of a real-time implicit approach," *IEEE/RSJ International Conference on Intelligent Robots and Systems (IROS)*, 2017.

[13] V. Duindam, A. Macchelli, S. Stramigioli, and H. e. Bruyninckx, *Modeling and Control of Complex Physical Systems - The Port-Hamiltonian Approach*. Springer, Sept. 2009.

[14] T. J. Courant, "Dirac manifolds," *Transactions of the American Mathematical Society*, vol. 319, no. 2, pp. 631–661, 1990.

[15] H.-S. Chang, U. Halder, C.-H. Shih, A. Tekinalp, T. Parthasarathy, E. Gribkova, G. Chowdhary, R. Gillette, M. Gazzola, and P. G. Mehta, "Energy shaping control of a cyberoctopus soft arm," in *2020 59th IEEE Conference on Decision and Control (CDC)*, 2020, pp. 3913–3920.

[16] A. van der Schaft and B. Maschke, "Hamiltonian formulation of distributed parameter systems with boundary energy flow," *Journal of Geometry and Physics*, vol. 42, pp. 166–194, 2002.

[17] Y. Le Gorrec, H. Zwart, and B. Maschke, "Dirac structures and boundary control systems associated with skew-symmetric differential operators," *SIAM Journal on Control and Optimization*, vol. 44(5), pp. 1864–1892, 2005.

[18] N. Liu, Y. Wu, and Y. Le Gorrec, "Energy-based modeling of ionic polymer–metal composite actuators dedicated to the control of flexible structures," *IEEE/ASME Transactions on Mechatronics*, vol. 26, no. 6, pp. 3139–3150, 2021.

[19] A. Macchelli and C. Melchiorri, "Modeling and control of the timoshenko beam.the distributed port Hamiltonian approach," *SIAM Journal on Control and Optimization*, vol. 43(2), pp. 743–767, 2004.

[20] R. Ortega, J. A. L. Perez, P. J. Nicklasson, and H. J. Sira-Ramirez, *Passivity-based control of Euler-Lagrange systems: mechanical, electrical and electromechanical applications*. London: Springer Verlag, 1998.
[21] R. Ortega and E. García-Canseco, "Interconnection and damping assignment passivity-based control: A survey," *European Journal of Control*, vol. 10, no. 5, pp. 432–450, 2004.
[22] E. Franco, J. Tang, A. G. Casanovas, F. R. y Baena, and A. Astolfi, "Position control of soft manipulators with dynamic and kinematic uncertainties," *IFAC-PapersOnLine*, vol. 53, no. 2, pp. 9847–9852, 2020, 21st IFAC World Congress.
[23] E. Franco, A. Garriga Casanovas, J. Tang, F. Rodriguez y Baena, and A. Astolfi, "Position regulation in cartesian space of a class of inextensible soft continuum manipulators with pneumatic actuation," *Mechatronics*, vol. 76, p. 102573, 2021.
[24] E. Franco, A. Garriga-Casanovas, J. Tang, F. Rodriguez y Baena, and A. Astolfi, "Adaptive energy shaping control of a class of nonlinear soft continuum manipulators," *IEEE/ASME Transactions on Mechatronics*, vol. 27, no. 1, pp. 280–291, 2022.
[25] Y. Yeh, N. Cisneros, Y. Wu, K. Rabenorosoa, and Y. Le Gorrec, "Modeling and position control of the hasel actuator via port-hamiltonian approach," *IEEE Robotics and Automation Letters*, vol. 7, no. 3, pp. 7100–7107, 2022.
[26] E. Cosserat and F. Cosserat, "Sur la théorie de l'élasticité. Premier mémoire," *Annales de la Faculté des sciences de Toulouse : Mathématiques*, vol. 1e série, 10, no. 3-4, pp. I1–I116, 1896.
[27] S. Antman, *Nonlinear Problems of Elasticity*, ser. Applied Mathematical Sciences. Springer New York, 2012.
[28] D. C. Rucker and R. J. W. III, "Statics and dynamics of continuum robots with general tendon routing and external loading," *IEEE Transactions on Robotics*, vol. 27(6), pp. 1033–1044, 2011.
[29] J. D. Till, *On the Statics, Dynamics, and Stability of Continuum Robots: Model Formulations and Efficient Computational Schemes*. University of Tennessee, 2019.
[30] R. Murray, Z. Li, S. Sastry, and S. Sastry, *A Mathematical Introduction to Robotic Manipulation*. Taylor & Francis, 1994.
[31] J. Linn, H. Lang, and A. Tuganov, "Geometrically exact cosserat rods with kelvin–voigt type viscous damping," *Mechanical Sciences*, vol. 4, pp. 79–96, 2013.
[32] A. van der Schaft, "Port-Hamiltonian modeling for control," *Annual Review of Control, Robotics, and Autonomous Systems*, 2020.
[33] V. Trenchant, H. Ramirez, Y. Le Gorrec, and P. Kotyczka, "Finite differences on staggered grids preserving the port-Hamiltonian structure with application to an acoustic duct," *Journal of Computational Physics*, 2018.
[34] D. Habineza, M. Zouari, Y. Le Gorrec, and M. Rakotondrabe, "Multivariable compensation of hysteresis, creep, badly damped vibration, and cross couplings in multiaxes piezoelectric actuators," *IEEE Transactions on Automation Science and Engineering*, vol. 15, no. 4, pp. 1639–1653, 2018.
[35] J. Caballeria, H. Ramirez, and Y. Le Gorrec, "An irreversible port-Hamiltonian model for a class of piezoelectric actuators," *IFAC-PapersOnLine*, vol. 54, no. 14, pp. 436–441, 2021, 3rd IFAC Conference on Modelling, Identification and Control of Nonlinear Systems MICNON 2021.
[36] D. Habineza, M. Rakotondrabe, and Y. Le Gorrec, "Bouc–wen modeling and feedforward control of multivariable hysteresis in piezoelectric systems: Application to a 3-dof piezotube scanner," *IEEE Transactions on Control Systems Technology*, vol. 23, no. 5, pp. 1797–1806, 2015.

Edgar Ayala Pérez was born in Aguascalientes, Mexico, in 1994. He received the Robotics engineering degree from the Universidad Autónoma de Aguascalientes in 2018 and in 2021 he obtained double master's degrees in Optomechatronics from the Optics Research Center in León, Mexico and in Automatic, Robotics and Control for Green Mechatronics from the University Bourgogne Franche-Comté in Besançon, France. His research interests include flexible structure control and port Hamiltonian system.

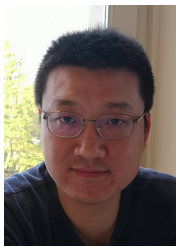

Yongxin Wu was born in Baoji, China in 1985. He received his engineer degree in Transportation Information and Control from the University of Chang'an, Xi'an, China in 2010 and his Master degree in Automatic Control from the University Claude Bernard of Lyon, Villeurbanne, France in 2012. He received his Ph.D. degree in Automatic Control in 2015 for his work on the model and controller reduction of port Hamiltonian systems at the Laboratory of Control and Chemical Engineering (LAGEP UMR CNRS 5007) of the University Claude Bernard of Lyon, Villeurbanne, France. From 2015 to 2016, He held a post-doctoral and teaching assistant position at LAGEP. Since 2016, he is an Associate Professor of Automatic Control at National Engineering Institute in Mechanics and Microtechnologies and affiliated to the AS2M department at FEMTO-ST institute (UMR CNRS 6174) in Besançon, France. His research interests include port Hamiltonian systems, model and controller reduction, modelling and control of multi-physical systems.

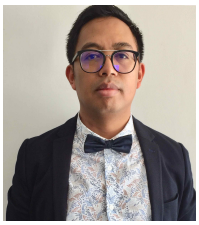

Kanty Rabenorosoa received the M.S. degree in electrical engineering from Institut National des Sciences Appliquées Strasbourg, Strasbourg, France, in 2007, and the Ph.D. degree in automatic control from the University of Franche-Comté, Besançon, France, in 2010. He was a Post-Doctoral Fellow at Laboratoire d'Informatique, de Robotique et de Micro-électronique de Montpellier, University of Montpellier, France, from 2011 to 2012. He is currently an Associate Professor with the AS2M Department, FEMTO-ST Institute, Besançon. His research interests include mechatronics, smart actuator, soft and continuum microrobotics for medical applications within the Micro-NanoRobotics team.

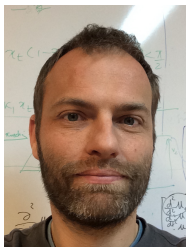

Yann Le Gorrec was graduated as engineer in "Control, Electronics, Computer Engineering" at the National Institute of Applied Sciences (INSA, Toulouse, France) in 1995. He received his Ph. D. degree from the National Higher School of Aeronautics and Aerospace (Supaero, Toulouse, France) in 1998. His field of interest was robust and self-scheduled control design. From 1999 to 2008, he was Associate Professor in Automatic Control at the Laboratory of Control and Chemical Engineering of Lyon Claude Bernard University (LAGEP, Villeurbanne, France). He worked the modeling and control of irreversible and distributed parameter systems with an application to physico-chemical processes. From september 2008 he is Professor at National Engineering Institute in Mechanics and Microtechnologies, and affiliated to the FEMTO-ST institute (UMR CNRS 6174), Besanç on, France. His main research activity is on port Hamiltonian formulations and their use for the modeling of multi-physical systems, model reduction, and control of non-linear and distributed parameter systems.